www.sciencemag.org/cgi/content/full/320/5879/1070/DC1

Supporting Online Material for

Anticorrelated Seismic Velocity Anomalies from Post-Perovskite in the Lowermost Mantle

Alexander R. Hutko, Thorne Lay,* Justin Revenaugh, Edward J. Garnero

*To whom correspondence should be addressed. E-mail: thorne@pmc.ucsc.edu

Published 23 May 2008, *Science* **320**, 1070 (2008)

DOI: 10.1126/science.1155822

This PDF file includes:

Materials and Methods
Figs. S1 to S6

Other Supporting Online Material for this manuscript includes the following: (available at www.sciencemag.org/cgi/content/full/320/5879/1070/DC1)

Movie S1

Anti-correlated Seismic Velocity Anomalies From Post-Perovskite in the Lowermost Mantle

Alexander R. Hutko[1†], Thorne Lay[1*], Justin Revenaugh[2], Edward J. Garnero[3]

[1]Earth and Planetary Sciences Department, University of California, Santa Cruz, CA 95064, USA. [2]Department of Geology and Geophysics, University of Minnesota, 310 Pillsbury Dr. SE, Minneapolis, MN 55455, USA. [3]School of Earth and Space Exploration, Arizona State University, Tempe, Arizona, 85287-1404, USA.
†Now at U.S. Geological Survey, MS 966 Box 25046, DFC, Denver, CO 80225
*To whom correspondence should be addressed. E-mail:thorne@pmc.ucsc.edu

Methods

The *P*-wave data processing for this study involved particularly careful event selection and equalization of signal shape so that many waveforms could be combined together to resolve weak reflections from the lowermost mantle. Seismograms were collected from regional short-period and broadband seismic networks in California, and deconvolved by their individual instrument response functions when available. Data from different instrument networks were processed separately, essentially as distinct events, to ensure that bandwidth differences do not affect the waveforms. Intermediate and deep focus earthquakes in South America were used, to minimize contamination from depth phases. Fig. S1 shows instrument-deconvolved *P* wave seismograms for a typical event. Only events with coherent, readily picked *P* arrivals like this were retained in the initial data screening. The data were then aligned on the *P*-arrival by cross-correlation or onset picking and summed to produce a source wavelet. This signal was then deconvolved from the seismograms by water-level deconvolution and the traces were Butterworth bandpass filtered in variable passbands of 0.25-0.5 Hz, 0.5-2.0 Hz and 0.1-2.0 Hz. The filtered traces were aligned and summed to produce a reference trace, which was cross-correlated with each filtered seismogram. The cross-correlation coefficient and a measure of signal-to-noise ratio were then used to reject noisy signals. This procedure gives rise to variation in number of traces for each passband, but ensures that only high quality, coherent signals are retained for subsequent processing.

The final data screening procedure, and perhaps the most important relative to earlier work, involved individual event stacking of the remaining data for each passband using a target depth range straddling the core-mantle boundary (CMB). If the data for a given event (for a specific instrument network) failed to form a coherent impulsive feature near the CMB that could be reliably associated with *PcP*, the event was discarded. This procedure ensures that the source wavelet deconvolution has successfully spiked-up phases that traverse the lowermost mantle including *PcP* and any precursory reflections, and that the radiation pattern is stable over the range of take-off angles and azimuths spanned by *P* and *PcP* raypaths from the source to the receivers. It is necessary to stack the data to do this, because unlike for *SH* signals, in which clear *ScS* arrivals can be seen in individual traces, *PcP* is often at or below the noise level due to its relatively low reflection coefficient at the CMB. A large number of events are excluded by this process, often being events with somewhat complicated source wavelets, but others being events that simply have particularly weak *PcP* arrivals. Shallower events with depth phases overlapping the *PcP* arrivals were also excluded.

One might be concerned that using *PcP* detectability as a criterion for data selection could bias interpretations of reflectivity of D″ structure, but this is not the case. Given that our data bins are extremely localized and many events show clear, impulsive *PcP* reflections in this region, the absence of such arrivals for paths sampling the identical region cannot be reasonably attributed to complexity at the CMB. Stacking all data with and without pre-screening for *PcP* detectability shows that the *PcP* stack shape is seriously corrupted by noisy data, even with thousands of traces being included, and this could lead to misinterpretation as a result of ultra low velocity zone structure or other complex mantle structure. Given that our final data set, after ensuring that all of our events have stable down-going energy to the lowermost mantle, is still far larger than previous investigations, we contend that this is the first study of *P*-wave signals in this region that can actually resolve the regional *P*-wave velocity structure.

The double-array procedure used to combine the accepted signals from all events into a single stack for each localized subregion is illustrated in Fig. S2. The IASP91 *P*-wave velocity model is used to compute the differential times of reflections from each target depth relative to the direct *P* time for each event-station pair. The sum of amplitudes at the corresponding time windows in the data are used to compute the strength of any reflectors at the target depths. Each waveform was normalized to have a peak *P* arrival with amplitude of unity, so the stack amplitudes are relative to *P*. When the data have a coherent arrival with move-out relative to *P* consistent with reflection from a given depth, the stack amplitude is high. Destructive interference causes the stack amplitude to be low at any target depth for which there is no coherent arrival. The bandwidth of the data determines how much smearing in depth occurs for any coherent arrival, thus the *PcP* image is spread over a finite depth range in Fig. S2. The depth at which a coherent arrival forms a stack image is an apparent depth, not the true depth, because the reference velocity model is only an approximation of the structure. By identical processing of synthetic seismograms for a specific velocity model and matching the features of the data stacks and the average *PcP-P* differential times, the absolute depths of structures in the deep mantle is determined correctly.

The main text emphasizes the *P*-wave stacks, as these are the major new data contribution of the paper. Several prior studies of *S*-wave signals in the study region have been performed, using a high quality data set that we re-model for this analysis. We begin with the data stacks from (20), for which the *S*-wave data have been deconvolved by stacks of the isolated *ScS* arrivals and low-pass filtered with a cut-off of 0.3 Hz. The data were then normalized and double-array stacked on *ScS* and *S* separately (Fig. S3), with the reference velocity structure for the stacking being PREM. Relative to the *P*-models, very strong *S* reflectors are observed at apparent depths of ~200 to ~300 above the CMB, and other secondary arrivals are observed at both shallower and deeper depths. Trial-and-error modeling of these stacks, allowing for multiple reflectors to match the features deemed significant was performed by (20), and the resulting models were slightly modified here in jointly fitting the *P* and *S* wave double array stacks. This yields the velocity models shown in Fig. S3, which contribute to the final models for each subregion given in Fig. 2.

There are lateral gradients in structure in all regions of the deep mantle, including across our study area, such that double-array stacking assuming 1D structure will fail to align some arrivals coherently. To reduce this effect, we use relatively small subregion bins, ensuring that all the data in a give stack sample within a Fresnel zone dimension (several hundred kilometers for our frequency bands), and we consider stacks aligned on direct phases (*P* or *S*) and on CMB-reflected phases (*PcP* or *ScS*). Since *PcP* is weak in individual traces, we pre-stack the data event by event, and determine shifts for each event that align the *PcP* arrival at the CMB. This reduces any errors caused by source mislocation or lateral gradients in structure affecting *PcP-P* differential times. The event shifts show a systematic pattern of increasing shift toward the north indicating higher V_p toward the north across our study area, as suggested by mantle tomography models (Fig. S4). The shifts are small, but when they are made, more coherent *PcP* stacks are found, with stronger *PcP*/*P* ratios. We compare stacks using both reference phases in Fig. S5a and Fig. S5b; our modeling emphasizes features that are stable for either choice.

The *P*-wave double array stacks for varying frequency bands, along with stacks for corresponding synthetics for our preferred subregion models are shown in Fig. S5. Our focus is on the 0.25-0.5 Hz passband, as this has the highest number of traces after quality control and the best signal-to-noise ratio, but our modeling was influenced by seeking to fit, or at least not violate, the noisier stacks for other passbands.

There is a trade-off between subregion dimensions and numbers of traces available to stack for a given subregion. Any choice involves some explicit lateral averaging of structure, and if small-scale heterogeneity is present, our final 1D models for a subregion will provide only an averaged value of the structure. To assess this, we subdivided each of our two subregions in half and stacked the smaller data sets for the four new subregions, using both *PcP* and *P* reference phases. The results, including stacks of synthetics for the two larger subregion models are shown in Figs. S5c and S5d. The stacks for the 2.5° wide bins with higher frequency data are significantly noisier than for the 5° wide bins, suggesting that the number of traces stacked is becoming too small for stability, but for the 0.25-0.5 Hz band there is good stability of the features that we concentrate on modeling for the 5° bins, indicating that it is valid to treat these as locally 1D. The one exception is for structure near 190 km above the CMB in the 10-15° range, where lateral variation of the depth of a small feature appears to average it out in the combined stack. The *S*-wave data set is too small to subdivide in this fashion, but we do observe an arrival near this depth in the 10-15° bin.

With the features that can be stably modeled with a 1D structure for each subregion being identified, we found our preferred models by trial-and-error modeling. The sensitivity of the models to strength of the velocity contrasts at the main discontinuities is demonstrated in Fig. S6, where synthetics for the favored models and for perturbed velocity contrasts are compared with the data. Features several hundred kilometers above the CMB are tightly constrained, but our resolution of structure closer to the CMB is limited due to interference with *PcP* and reduced sensitivity of the data for pre-critical reflections. We include comparisons with velocity models found in earlier studies (Fig. S6d), showing that those studies give poor agreement with the structure 320 km above the CMB, but reasonable agreement for the structure near 190 km above the CMB.

While the path coverage for our study area is limited to a narrow corridor, the assumption of localized 1D behavior can be further tested by performing a 3D migration. This was done using a point-scattering formulation, in which a 3D grid of possible scattering locations in a large lower mantle volume is defined, and all data are combined in a migration that allows for pre-critical scattering from each point. A reference velocity model (IASP91) is selected, and relative to the *P* arrival for a given source-receiver combination, differential arrival times from each scattering location are computed. The seismograms are then shifted and summed in order to detect any coherent scattered arrival from that position at the correct time in all waveforms. The

3D volume of scattering strengths is then visualized to evaluate where viable scattering structures may be located. Spatial isolation of scatterers is limited due to the non-uniform ray coverage, and specular reflections from horizontal boundaries form laterally continuous features with diffraction smiles on their edges. By making synthetic seismograms for each path in the data set and processing the synthetics with the same migration, all of the sampling artifacts can be accounted for. The on-line movie (Movie S1) provides a sequence of cross-sections through the migration volume for the data, for a merged synthetic waveform set for the preferred models, and for a simple 1D Earth model (IASP91). The cross-sections parallel the corridor sampled by the raypaths. Cross-sections offset to the SW or to the NE from the *PcP* reflection points show features formed mainly from *PcP* and other reflections at depths above their true turning points (edges of the diffraction smiles). To enhance the weaker arrivals and to suppress any contamination from *PcP*, we also show the migration results with *PcP* masked out by tapering the waveforms to zero amplitude around the *PcP* arrival time. The profiles close to the average great-circle plane through the CMB reflection points correspond to the region for which the 1D double-array stacks were computed, and clear features are seen near 320 km and 190 km above the CMB as expected (Fig. 3). Note that the shallower feature is well-explained by our models, and the 190-km feature is largely due to a change in velocity gradient like that in the IASP91 (or PREM) models near this depth, enhanced by a small 0.2-0.4% V_p discontinuity in our preferred models.

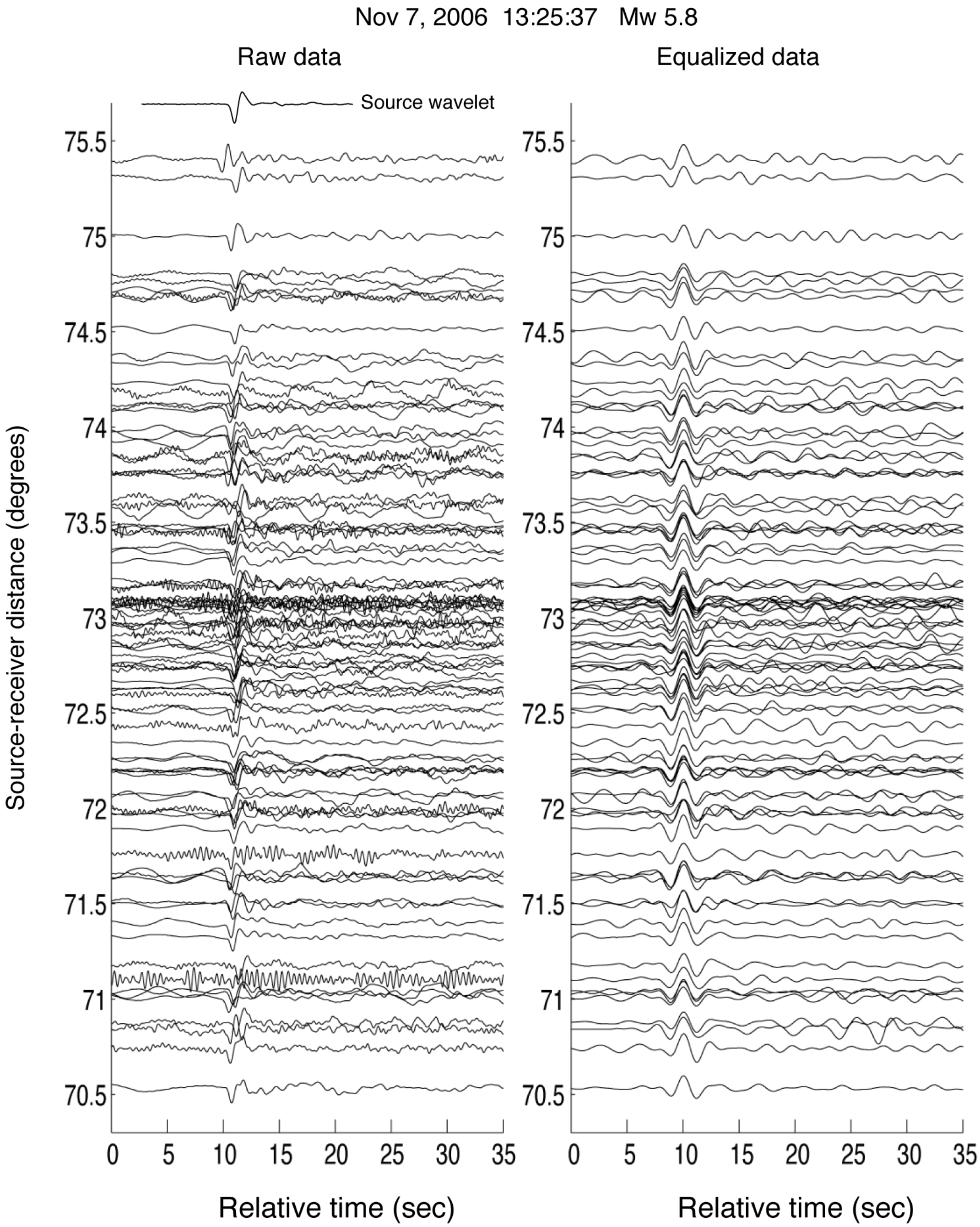

Fig. S1. Instrument-corrected *P*-wave seismograms for an event on November 7, 2006 (left) aligned on theoretical arrival times and stacked to give (top left) an average source wavelet, then (right) deconvolved by the source wavelet and aligned on peak arrivals and narrow band filtered from 0.25-0.5Hz. The raw data were individually inspected for sufficient signal-to-noise ratio and stability of the *P*-wave shape then aligned on the first arrival before stacking to estimate the source wavelet. Deconvolution of source wavelets for each event equalizes the data for the double-array stacking procedure. The traces on the right were summed to form a master trace, and the cross-correlation coefficient between individual traces and the master trace along with signal-to-noise ratio were used as criteria to discard traces.

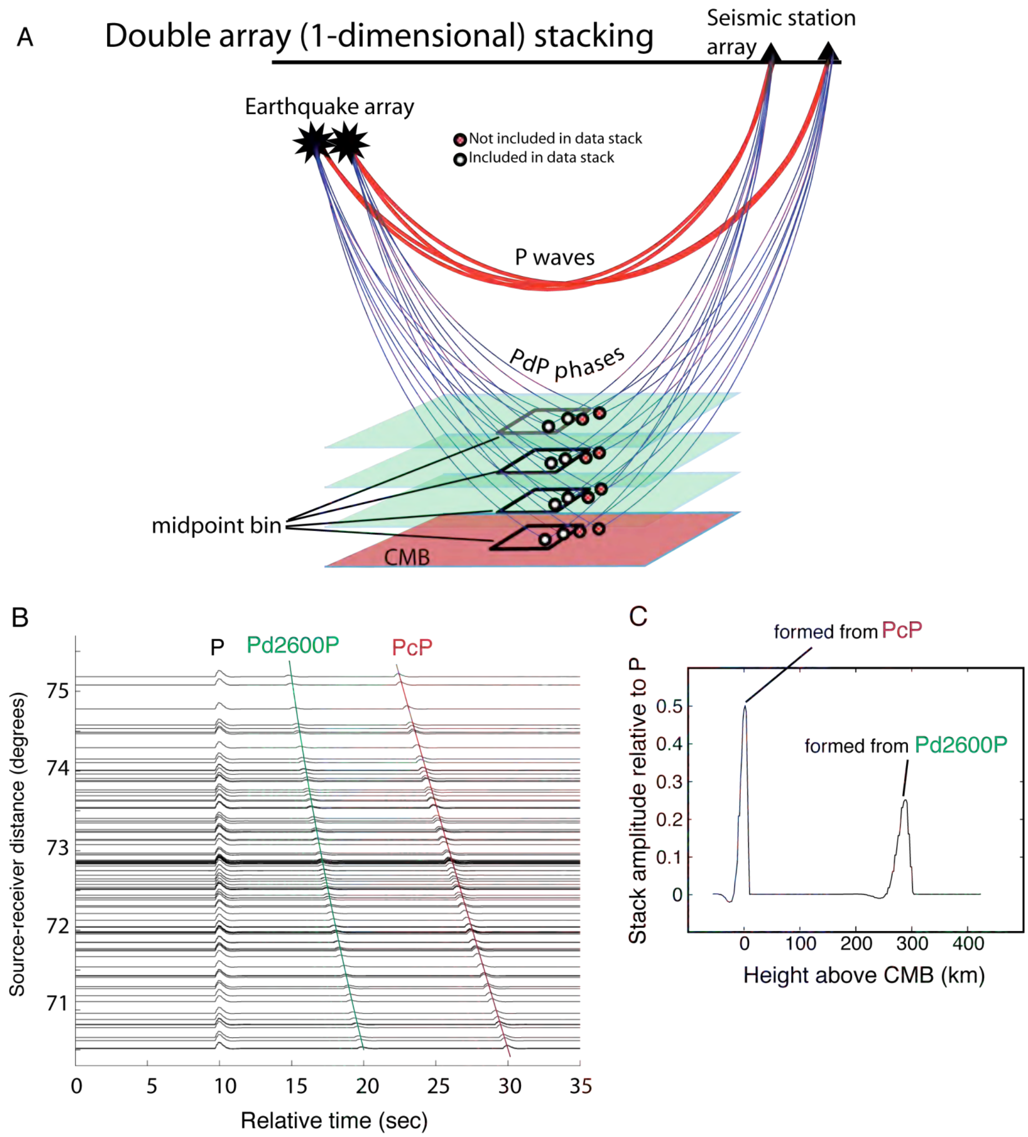

Fig. S2. (A) A schematic indicating the nature of double array stacking, which seeks to find any energy from locally flat specular reflectors within a specified depth range relative to a reference depth (here the CMB) using waveforms from arrays of both sources (earthquakes) and receivers. Data are binned based on having CMB reflection points spanning the ~300 km wide subregions, with the assumption being that structure does not vary laterally over corresponding scale length. (B) For a given earthquake, data are aligned on the direct *P*-wave in order to account for travel time variations due to lateral crustal and upper mantle velocity heterogeneities. For a given target depth, such as 2600 km, the travel times for reflection from that depth for a specified reference velocity model (IASP91) for each source-receiver pair is calculated (in this case, the synthetic waveforms do have a reflection from 2600 km depth, labeled *Pd2600P*). The data are then linearly summed along this resulting travel time curve (green line). This process is repeated for many target depths. (C) The resulting double array stack as a function of target depth shows the stack amplitudes normalized relative to *P*, with the relative amplitudes and inferred depths of reflectors (*PcP* from the CMB and *Pd2600P* from 2600 km depth) being well resolved, as long as the reference velocity model is reasonably accurate.

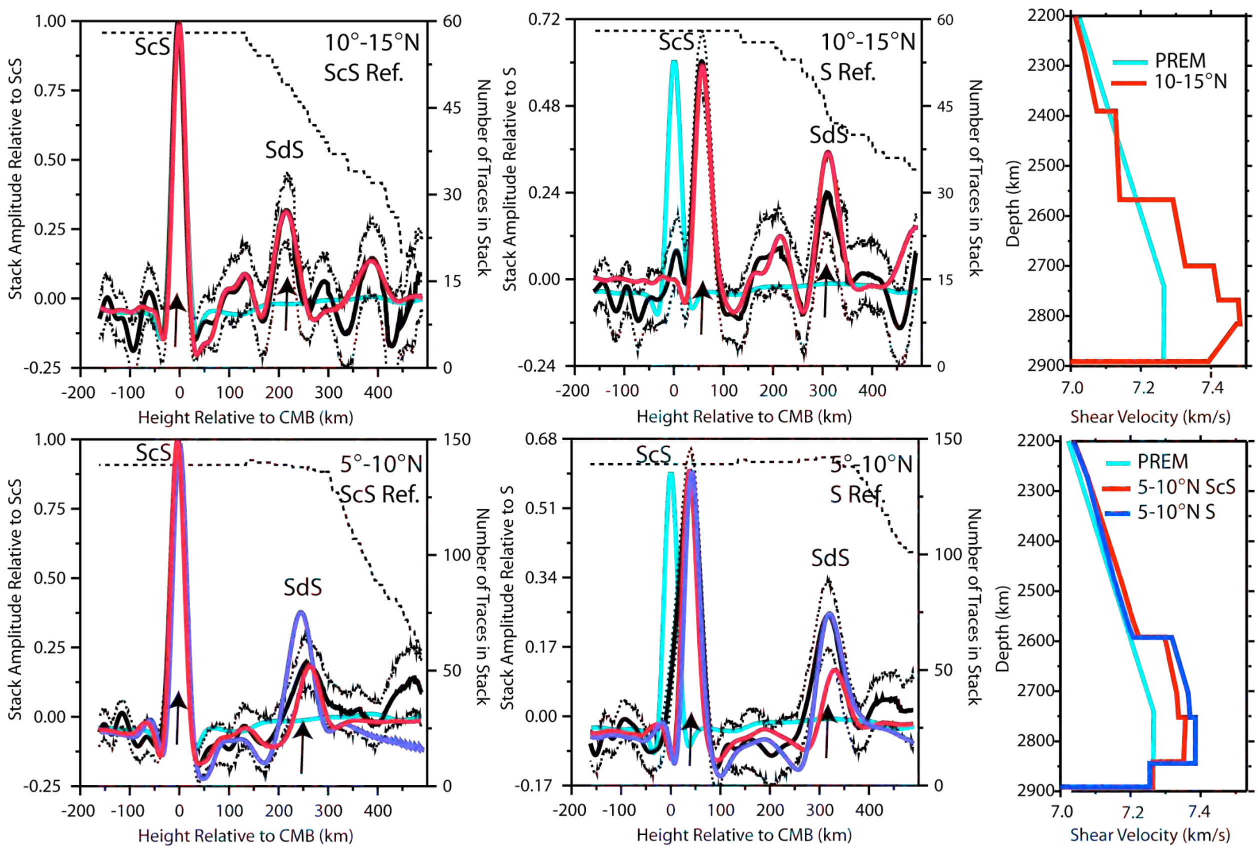

Fig. S3. Double array stacks of *S*-waves, along with models slightly modified from those in (20). Stacks on the left are for alignment on *ScS* as a reference phase while those in the middle are for alignment on *S* as a reference phase. The amplitude of the data stack at various target depths relative to the CMB is shown (bold black lines, left vertical-axes), along with bootrstrap-estimated variance of the stack (dotted black lines). Arrows indicate the *ScS* and *SdS* features. Short dashed lines indicate the number of traces contributing to the stack at each target depth (right vertical-axes). Red, blue and cyan lines corresponding to stacking of synthetics for the corresponding color-coded velocity models shown on the right, fit by trial-and-error to the data, along with model PREM, which has no *SdS* reflection.

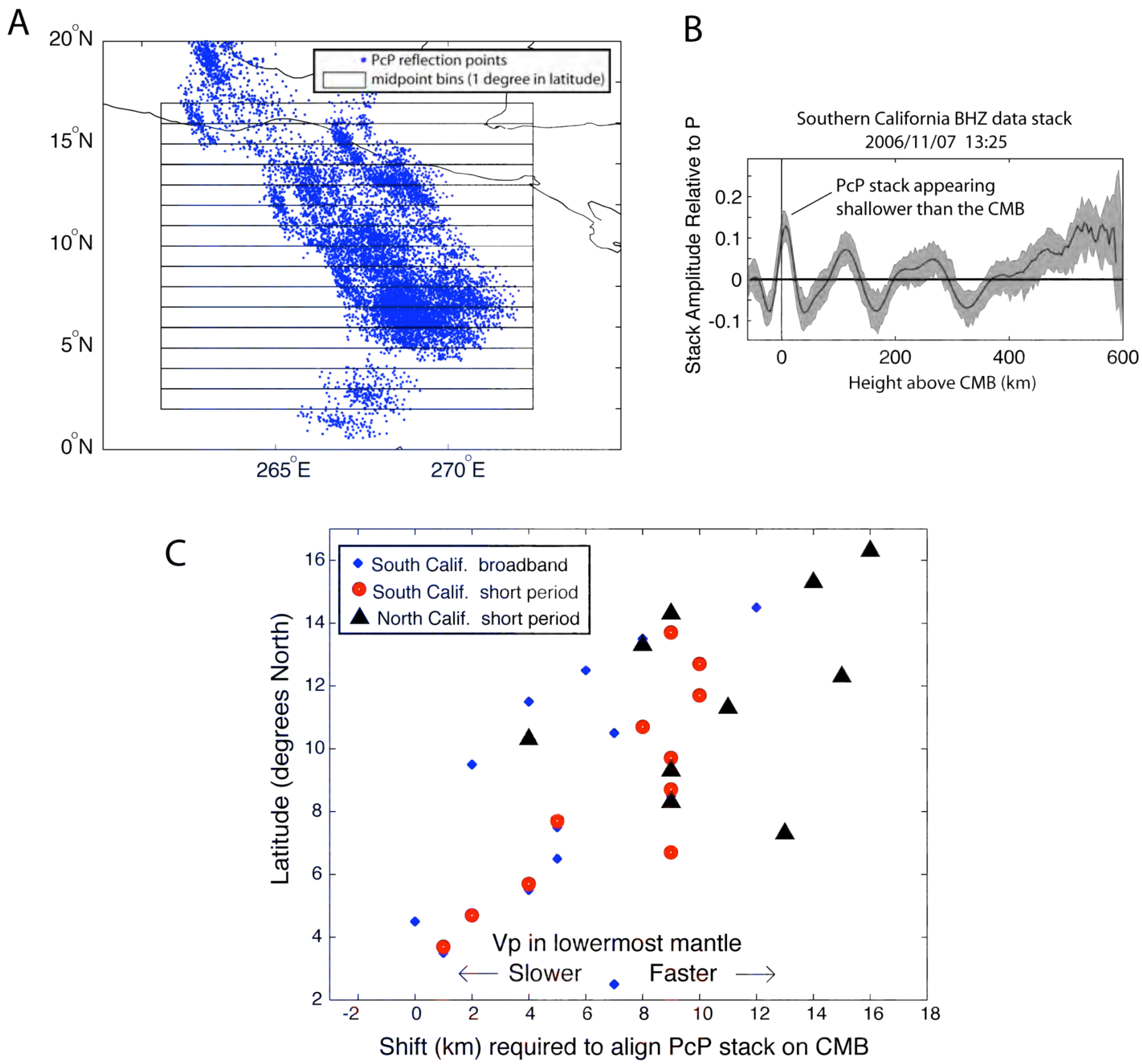

Fig. S4. (A) Map showing 1° bins used to compute double array stacks for our *P*-wave data to constrain V_p variations. (B) An example event stack showing an 8 km too shallow apparent depth for the *PcP* reflection, which indicates higher V_p in the deep mantle than in the reference model, or errors in source depth or travel time anomalies in *P* arrivals. (C) The apparent depth shifts of the *PcP* images in the 1° bin stacks determined for each waveform set (Southern California broadband, Southern California short-period and Northern California short-period). The trend of the shifts indicates increasing V_p in the lowermost mantle toward the north, consistent with previous studies (8). Some of the scatter may represent source depth errors. Effects of this velocity variation on the double-array stacks are suppressed by aligning the *PcP* features for all events on the CMB, and by comparing the stacks aligned on *PcP* with stacks aligned on *P*.

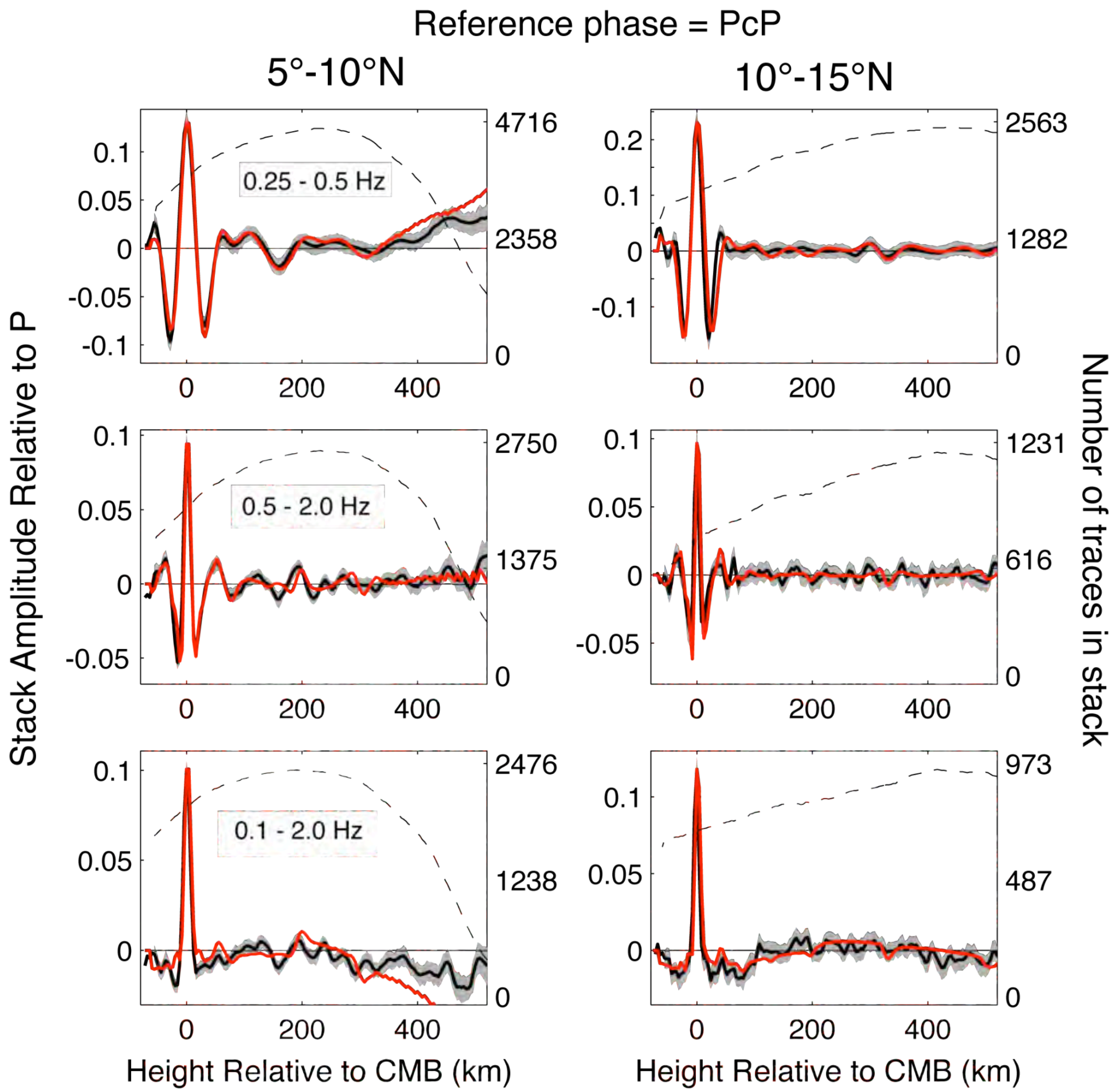

Fig. S5a. Comparison of *P*-wave double array stacks for data and final model synthetics with *PcP* aligned event by event at the CMB for three frequency bandwidths: 0.25-0.5 Hz, 0.5-2.0 Hz and 0.1-2.0 Hz. Signal quality was evaluated for each passband, leading to varying number of traces in each stack. The 0.25 – 0.5 Hz stacks have the highest signal-to-noise ratios, and largest number of contributing seismograms from the combined broadband and short-period networks. We focus our forward modeling efforts on the 0.25 – 0.5 Hz band since it has the highest signal-to-noise (*PdP*/*PcP*) ratio. However, the other bandwidths provide additional constraints on the model velocity structures. The data bin from 5-10°N is sampled by signals at slightly larger distances from the stations than the 10-15°N bin, which is sufficient to cause differences in the data stacks for a given model. Thus, the relatively strong *P*-wave reflectivity near 180 km above the CMB in the 5-10° bin is not inconsistent with the absence of corresponding reflectivity in the 10-15°N bin.

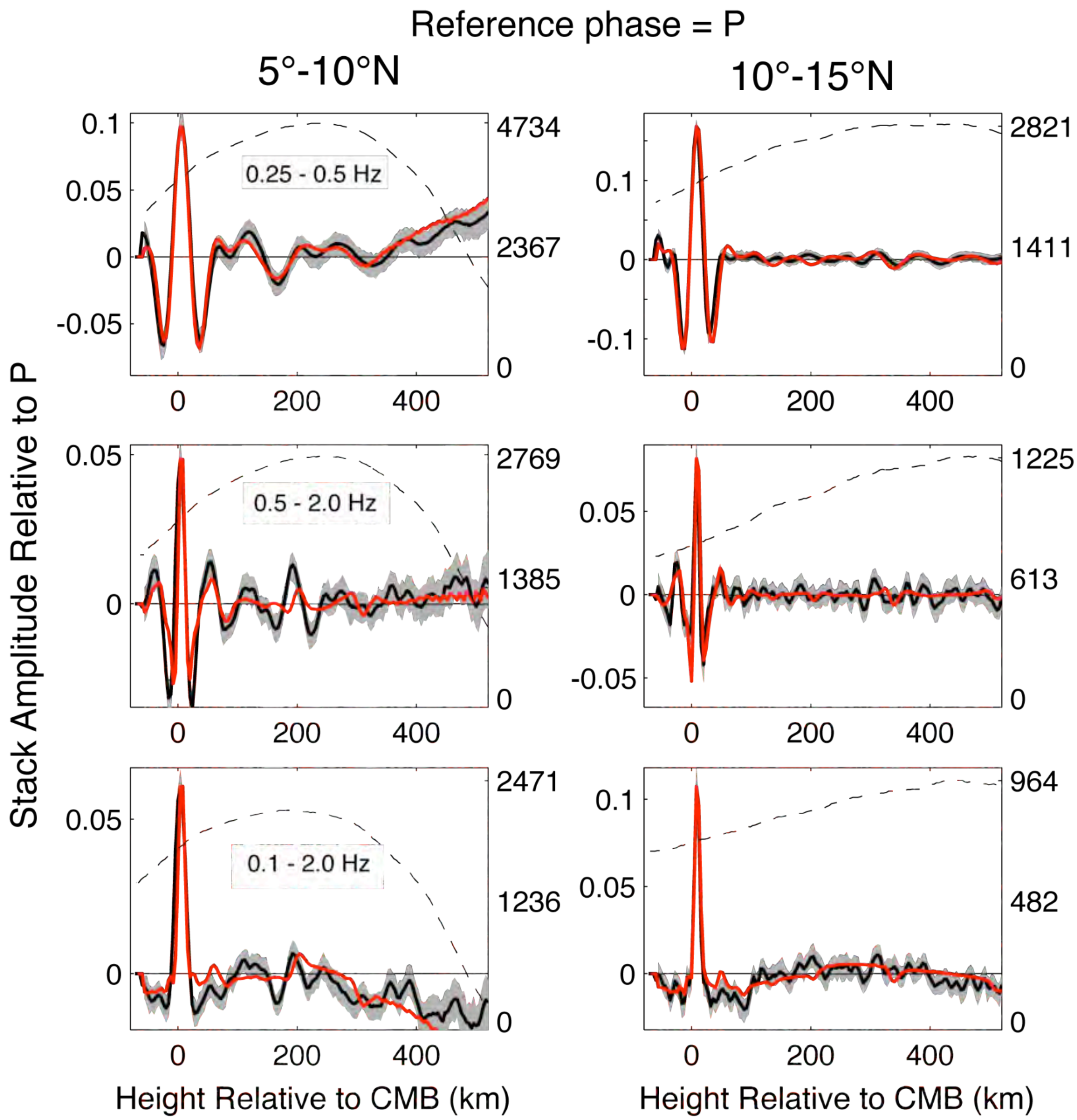

Fig. S5b. Like Fig. S5a, but with data aligned on *P* (i.e. event stacks were not shifted to place the stack of *PcP* at the CMB). Note the slight reductions of the *PcP* stack amplitude when aligned relative to *P*. This is caused by variability in differential timing from event to event due to either source depth error or volumetric heterogeneity. The similarity between stacks using the two different reference phases (especially for the 0.25 – 0.5 Hz bandwidth) suggest that lateral V_p variations are relatively minor, and our preferred models are not dependent on the choice of reference phase.

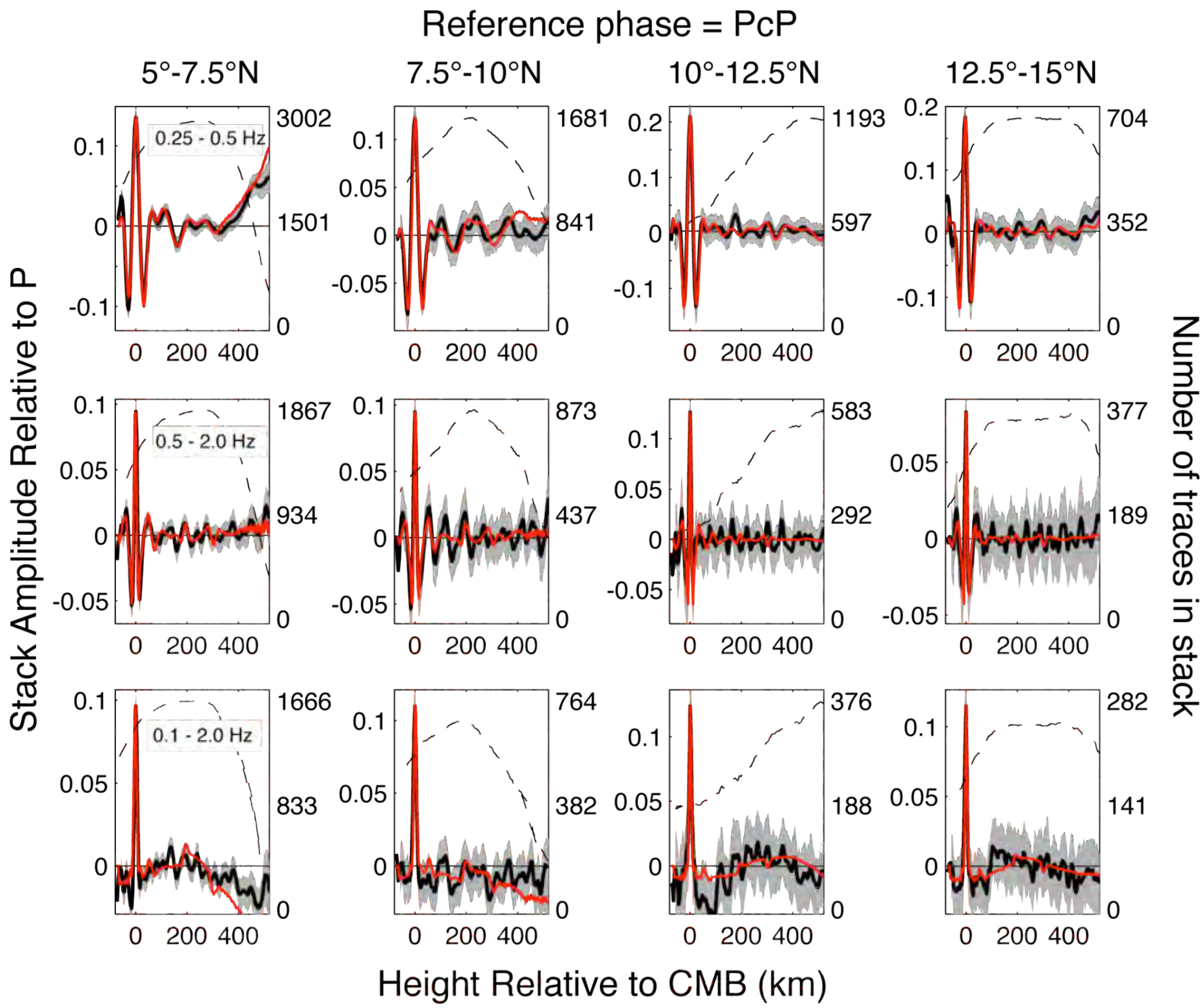

Fig. S5c. Similar to Fig. S5a, but with the bin latitude ranges being only 2.5°. This reduces the number of data contributing to the stacks and noise in the stacks increases, but there is still good stability of the lower frequency stacks, and the preferred subregion models predict the individual bins adequately. Some incoherence in the two northern stacks is present in the depth range 200-300 km above the CMB, which is not fully accounted for by our preferred models.

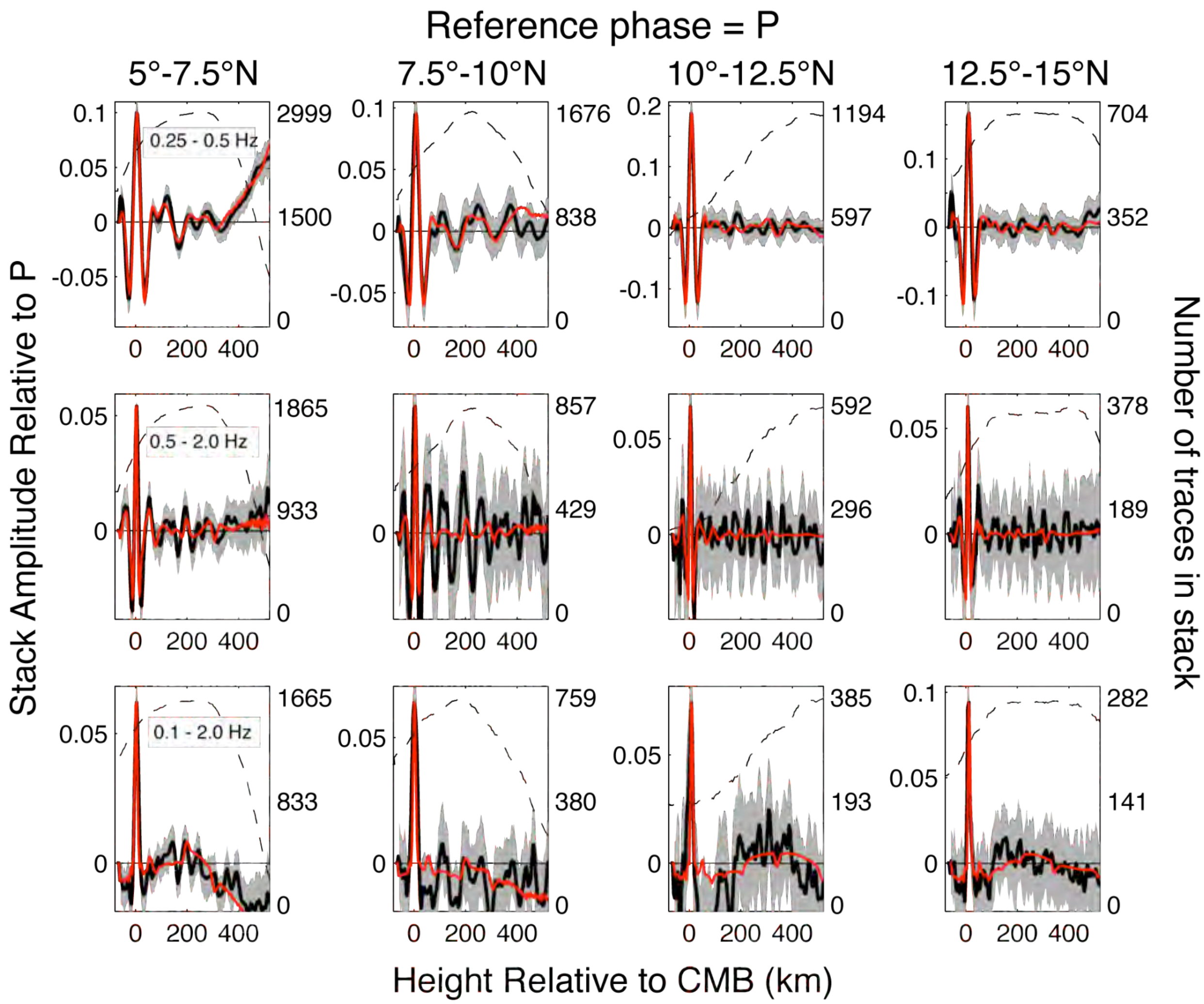

Fig. S5d. Similar to Figure S5c, but for stacks with *P* used as a reference phase.

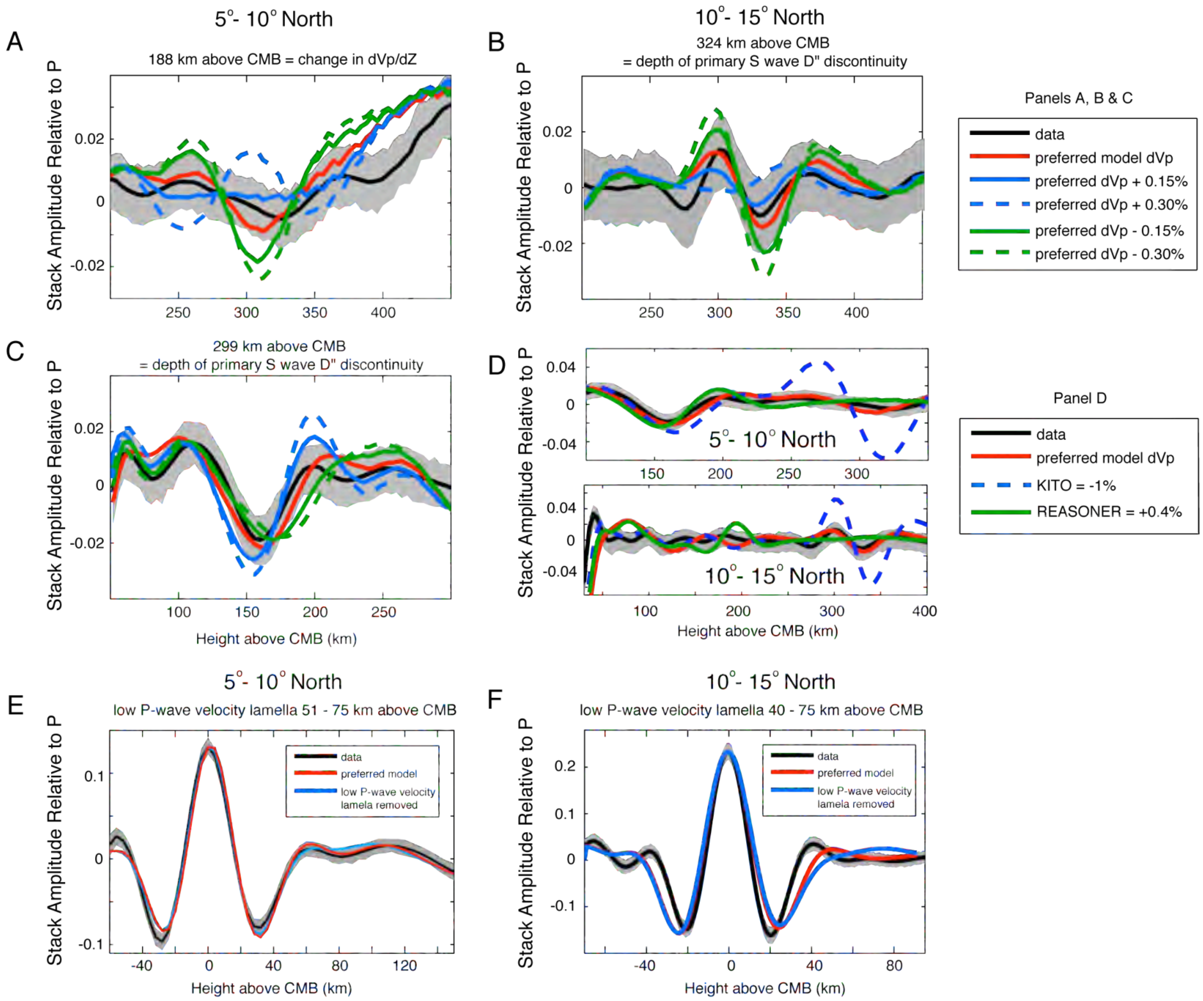

Fig. S6. Sensitivity of *P*-wave double array stacks to perturbations from the preferred models. (A) Comparison of data and synthetics for the 5-10° bin near depths 188 km above the CMB. (B) Comparison of data and synthetics for the 10-15°bin near depths 324 km above the CMB. (C) Comparison of data and synthetics for the 5-10° bin near depths 188 km above the CMB. (D) Comparisons of data with predictions for models from prior studies in the region. In each case, the red line is for the double array stack of synthetics made with our preferred model, which provides our best fit to the data. The blue solid and dashed lines represent increases to the velocity jump in the preferred models of only 0.15% and 0.3%, respectively, while the green lines show the effect of decreasing the velocity jump corresponding amounts. For example, in (A) the *P*-wave velocity of the preferred model has an increase of +0.2%. The solid green line thus is for stacks of synthetic seismograms made with a model where the increase in *P*-wave velocity is only +0.05%. If the velocity increase of 0.2% is distributed across 20 km in depth, the fits to the model become significantly poorer in the 0.5 – 2.0 Hz band (not shown), suggesting that the increase in velocity must occur over less than 20 km in depth. (E and F) Our preferred models (red lines) include a low velocity lamella in the basal layer, which slightly improve the fits to the data stack relative to models without the lamella (blue lines).

Movie in separate file.

Movie S1. Animation of a suite of cross-sections through the migration volume for the data (left column), synthetics for the preferred velocity models (second column) and synthetics for the IASP91 reference model (third column) (one cross section is shown in Fig. 3). The map in the upper-right shows the relative location of the great circle path along which the cross-section is made (heavy black line), the location of the *PcP* CMB reflection points for the data set (blue dots) and the maximum number of seismograms contributing to the migration images along each great circle path. The map at the bottom-right shows the number and relative location of earthquakes that contributed to the data set used to form these images. The color scales are held constant for all sections. The dominant feature in the upper row (the CMB reflector formed by *PcP* arrivals) appears shallower along great circle paths that are out of the dominant source-receiver plane, i.e. on profiles offset from where the CMB reflection points are. This is a result of the scattering ellipsoids not having destructive interference due to the limited azimuthal sampling provided by the data corridor. The raypaths through D" of our data set are at near grazing-angles and thus there is lateral streaking as in the *S*-wave migrations of (13).